processes

MDPI

Article

Reliable Wind-Turbine Performance Prediction Using a Modular Corrected Blade-Element Momentum Framework

Tao Zhang [1], Mohammed Djamel Eddine Boudjelkha [1,*], Abdelhamid Bouhelal [2,3], Saleh Mahamat Aboubakar Ousmane [1] and Sarkar Mohammad Raziul Hasan Rifat [1]

[1] Faculty of Mechanical and Material Engineering, Huai'an University, Huai'an 223003, China; taozhang2021@hau.edu.cn (T.Z.); slam.saleh141@gmail.com (S.M.A.O.)
[2] Department of Mechanical Engineering, Faculty of Technology, University of El Oued, El Oued 39000, Algeria; bouhelal-abdelhamid@univ-eloued.dz
[3] Laboratory of Green and Mechanical Development (LGMD), Ecole Nationale Polytechnique (ENP), B.P. 182, El-Harrach, Algiers 16200, Algeria
* Correspondence: djamelmoh3904@gmail.com

Abstract

Post-stall prediction of wind turbine performance remains challenging because momentum corrections, rotational augmentation, and high-angle airfoil treatment interact, obscuring their individual contributions to global and sectional accuracy. This study develops a modular blade-element momentum (BEM) framework that evaluates these contributions through a common-input correction hierarchy for the NREL Phase VI rotor. Six configurations combine Prandtl and Buhl corrections, Snel or Chaviaropoulos–Hansen (CH) augmentation, and full-angle or endpoint-clamped polars. Predictions are assessed against digitized experimental torque and sectional coefficients at seven wind speeds from 5 to 25 m s^{-1}, with radial refinement analysis and an external SimRotor comparison. Prandtl–Buhl–CH reduces torque and aerodynamic power root mean square errors by 76.5% relative to the two-dimensional baseline, to 204.2 N m and 1.539 kW, respectively. The chord-normal coefficient error decreases by approximately 70.0%, to 0.163, with $R^2 = 0.908$. CH's twist-dependent attenuation and coupled lift and drag augmentation support improved spanwise load retention, while the full-angle polar yields substantially lower errors than endpoint clamping. However, Snel gives lower mean absolute error, and CH retains a chord-tangential error of 0.134 with $R^2 = -2.114$. These findings identify rotational augmentation and polar closure as major controls on post-stall performance, while demonstrating that improved integrated predictions do not ensure uniformly accurate sectional loads. Source code, input data and comparison outputs are provided as Supplementary Material.

Keywords: horizontal-axis wind turbine; blade-element momentum; NREL Phase VI; rotational augmentation; stall delay; Viterna extrapolation

Check for updates

Academic Editor: Shen-Haw Ju

Received: 17 September 2026
Revised: 9 October 2026
Accepted: 21 October 2026
Published: 27 October 2026

Copyright: © 2026 by the authors. Licensee MDPI, Basel, Switzerland. This article is an open access article distributed under the terms and conditions of the Creative Commons Attribution (CC BY) license.

1. Introduction

Horizontal-axis wind turbines operate over a broad range of aerodynamic regimes, from attached flow near rated conditions to highly separated post-stall flow under large wind speeds, start-up transients, or control-limited operation. During the early and intermediate design stages, the aerodynamic model must be sufficiently fast for parametric studies and optimization, while remaining accurate enough to predict the influence of chord distribution, twist distribution, pitch, airfoil polar quality, and operating point. This compromise explains the continued central role of blade-element momentum theory in wind turbine analysis

and design [1–4]. Recent studies continue to refine the method through CFD-informed assessments of tip/root-loss, stall-delay and high-thrust closures, confirming that correction-model selection remains a principal source of BEM uncertainty [5–7].

Blade-element momentum (BEM) theory combines a one-dimensional momentum balance over annular streamtubes with two-dimensional airfoil section data. The method is computationally efficient because it avoids resolving the full three-dimensional flow field. However, this efficiency is obtained through simplifying assumptions: annular elements are treated as weakly coupled or independent, the wake is represented through induction factors, and local aerodynamic forces are inferred from airfoil polars. Consequently, the quality of a BEM prediction depends strongly on the correction models used to represent effects that are absent from the ideal actuator-disk and two-dimensional blade-element assumptions. Modern extensions also seek consistent links between BEM loading and actuator-based turbine models while retaining negligible additional computational cost [8].

Several correction classes are required when BEM is applied to real rotors. Prandtl-type loss factors reduce the momentum loading near the tip and hub where finite blade number and vortex roll-up invalidate the infinite-blade assumption [9], although recent CFD-based assessments show that conventional loss formulations can overpredict tip-region loading, and that load-dependent corrections can improve the tangential force prediction [5,6]. High-induction corrections are necessary when the classical momentum relation enters the turbulent windmill state and no longer provides a physically reliable axial induction factor [7,10]. Rotational augmentation models account for delayed separation and enhanced lift on rotating blades, especially in the inboard and mid-span regions where the chord-to-radius ratio is large [11–15]. Finally, polar extrapolation is required because a BEM iteration frequently demands lift and drag coefficients at angles of attack beyond the measured airfoil database, particularly in post-stall operation [14,16,17].

The National Renewable Energy Laboratory (NREL) Unsteady Aerodynamics Experiment Phase VI rotor is a rigorous benchmark for assessing these correction models. The rotor has a well-documented twisted and tapered blade equipped with the S809 airfoil and was tested under controlled conditions in the NASA Ames wind tunnel. The database includes rotor scale quantities as well as pressure-derived sectional information, allowing validation to move beyond a simple power-curve comparison [18,19]. This distinction is important because integrated torque or power can be reproduced by compensating errors distributed along the span, whereas sectional normal and tangential force coefficients expose the local aerodynamic quality of the model. Recent stalled-rotor simulations likewise show that local wake and sectional load comparisons reveal deficiencies that may not be apparent from integral performance alone [15].

The main difficulty in the Phase VI benchmark is the transition from attached or mildly separated flow to stall-dominated operation as the wind speed increases. A BEM model based only on 2D airfoil data generally loses too much lift after static stall and underpredicts torque in the post-stall region. Momentum corrections alone can improve the induction solution, but they cannot correct the sectional lift deficit produced by the use of stationary airfoil polars on a rotating blade. A physically consistent engineering model must therefore combine momentum-side corrections with airfoil-side rotational augmentation and a robust post-stall polar closure [5,14,15].

Recent developments include an engineering stall-delay model evaluated against Navier–Stokes calculations and measurements [20], a machine-learning extension of BEM [21], and uncertainty quantification of BEM predictions [22]. Together with experimental characterization of unsteady stall [23], these studies motivate distinguishing correction-model sensitivity from input uncertainty and flow phenomena beyond steady polar-based modeling.

This study contributes a modular implementation and a combined rotor scale and sectional assessment of established BEM corrections. Independently selectable momentum corrections (Prandtl/Buhl), sectional lift and drag augmentation (Snel/CH), and high-angle polar treatments allow incremental effects to be evaluated under common inputs. The six-configuration hierarchy examines selected combinations; the aerodynamic and momentum responses remain coupled through induction. Radial refinement, consistent force projections and operating point error analysis support a reproducible assessment of the NREL Phase VI rotor under steady axial inflow.

2. Materials and Methods

2.1. Experimental Benchmark and Validation Database

The numerical study is based on the standard-tip upwind NREL Phase VI rotor operating in axial inflow. The turbine has two blades, a tip radius of 5.029 m, a hub radius of 0.5083 m, a fixed rotational speed of 72 rpm, and a blade tip pitch of 3 deg. The blade is tapered and twisted and uses the S809 wind turbine airfoil. The aerodynamic blade span is discretized from r = 1.2575 m to the blade tip using 2880 annular elements. Chord and twist are interpolated by a shape-preserving cubic scheme in order to avoid artificial oscillations in the inboard region. The numerical configuration is summarized in Table 1.

Table 1. Numerical configuration used for corrected BEM simulations.

Parameter	Value
Rotor	NREL Phase VI standard-tip upwind rotor
Airfoil	Clean S809, Re = 750,000; archived full-angle PCHIP table
Number of blades	2
Tip radius	5.029 m
Hub radius	0.5083 m
Aerodynamic span	1.2575 m <= r <= 5.029 m
Rotor speed	72 rpm
Blade tip pitch	3 deg
Yaw angle	0 deg
Wind speeds	5, 7, 10, 13, 15, 20 and 25 m s^{-1}
Air density	1.225 kg m^{-3}
Dynamic viscosity	1.7894×10^{-5} kg m^{-1} s^{-1}
Radial discretization	2880 uniform annuli; midpoint integration; refinements to 11,520
Polar treatment	Archived full-angle table (±180°); endpoint-clamped sensitivity
Convergence	Update and fixed-point residual $< 10^{-8}$; maximum 1000 iterations
Relaxation	0.35 for a and a′; initial a = 0.3, a′ = 0
Prandtl floor	Fmin = 10^{-4}; sine floor 10^{-5}

The validation dataset comprises digitized experimental markers in Huque et al. [24]: Figures 35–41 give chord-normal and chord-tangential coefficients at 5, 7, 10, 13, 15, 20, and 25 m s^{-1}, and Figure 42 gives rotor torque. The five comparison coordinates are r/R = 0.300, 0.467, 0.633, 0.800 and 0.950, giving 35 points per coefficient. The nominal second instrumentation station is 0.466 in the campaign report [18]; 0.467 is the source figure coordinate retained by the solver. Reported conditions are standard-tip geometry, axial inflow, 3° pitch, and 72 rpm, consistent with the Sequence S configuration. The secondary figures do not identify raw campaign filenames, torque channel or averaging windows. Table 2 lists the rotor scale observations; power is calculated from torque, not independently measured. Five stations support comparisons at sampled locations rather than continuous spanwise validation.

Table 2. Rotor scale experimental validation data.

$U\ [m\ s^{-1}]$	$Q_{exp}\ [N\ m]$	$P_{exp}\ [kW]$	$C_{P,exp}\ [-]$
5	260	1.960	0.3223
7	780	5.881	0.3523
10	1335	10.066	0.2068
13	1385	10.443	0.0977
15	1180	8.897	0.0542
20	1110	8.369	0.0215
25	1490	11.234	0.0148

2.2. Validation Data Uncertainty

At each primary station, the campaign uses 22 pressure taps, concentrated near the leading edge [18]. Pressure integration excludes skin friction and depends on tap coverage, calibration, and the treatment of uninstrumented chord intervals. Centrifugal pressure corrections and corrected stagnation normalization QNORM enter the measured coefficients. The campaign also documents a roughly 10% local pressure-coefficient discrepancy at the 0.5%-chord upper tap, attributed to positioning or interference; its small integration area limits the effect on sectional force. This is a local sensor observation, not a 10% uncertainty on all integrated loads. Tubing response and finite time averaging can affect separated-flow fluctuations; a steady coefficient comparison cannot test that response.

Repeated marker-center selections and axis-calibration records are unavailable for the digitized dataset, preventing estimation of a digitization confidence interval. For a linear source axis spanning Δy over H pixels, a marker-location bound of $\pm k$ pixels propagates as $\pm k\Delta y/H$. Torque, wind speed, pressure calibration, tubing response, integration and digitization uncertainties must be distinguished. Their quantitative combination requires the selected raw channels, calibration records and covariance, which are not encoded in the secondary arrays. Accordingly, numerical precision in the tables is for reproducibility; it is not experimental accuracy, and no experimental uncertainty bars are inferred from sensor resolution alone.

Power and torque are not independent validation measurements here because $P = \Omega Q$. For uncorrelated Q and Ω, $[u(P)/P]^2 = [u(Q)/Q]^2 + [u(\Omega)/\Omega]^2$. For $C_P = P/(\rho A U^3/2)$, independent relative contributions add as $[u(C_P)/C_P]^2 = [u(P)/P]^2 + [u(\rho)/\rho]^2 + [u(A)/A]^2 + 9[u(U)/U]^2$. These expressions describe propagation, not uncertainty values established for the digitized dataset. Source traceability and quantitative intervals are needed before claiming that the CH–Snel difference is statistically resolved.

2.3. Airfoil Inputs and Reynolds Number Dependence

The exact 58-row input table matches the archived S809_Cln.dat coefficients [25]. Its header identifies clean Ohio State University data at $Re = 7.5 \times 10^5$, with Viterna extension using aspect ratio 11. The central input interval is $-20.1° \leq \alpha \leq 20.1°$; the full tabulation spans $-180°$ to $180°$. The nominal Reynolds field of 9.9×10^9 in the legacy file is a sentinel for a single table, not the experimental Reynolds number. Shape-preserving piecewise cubic Hermite interpolation (PCHIP) is used for geometry and coefficients. One fixed-Re polar is used at all radii and speeds: the calculated Re is diagnostic and does not update coefficients. The refined calculations span approximately 0.540×10^6 to 1.300×10^6. Transition, drag, and separation may therefore differ from the fixed-Re inputs, especially near stall, and the present correction ranking cannot isolate that uncertainty.

3. Corrected Blade-Element Momentum Formulation

For each annular element, the solver iterates the axial induction factor a and tangential induction factor a′ until the blade-element forces and momentum balance are mutually consistent. The local solidity is

$$\sigma(r) = \frac{Bc(r)}{2\,pi\,r} \tag{1}$$

The axial and tangential velocity components seen by the rotating blade section are

$$U_a = U_\infty(1-a),\ U_t = \Omega\, r\,(1+a') \tag{2}$$

The inflow angle, relative velocity, and angle of attack are then evaluated as

$$\phi = atan2[U_\infty\,(1-a),\ \Omega\, r(1+a')] \tag{3}$$

$$W = \sqrt{[U_\infty(1-a)]^2 + [\Omega\, r\,(1+a')\,]^2} \tag{4}$$

$$\alpha = \phi - \theta,\ \theta = \theta_{tw} + \beta \tag{5}$$

The interpolated or extrapolated airfoil coefficients are projected into directions normal and tangential to the rotor plane:

$$C_N = C_l\, cos(\phi) + C_d\, sin(\phi) \tag{6}$$

$$C_t = C_l\, sin(\phi) - C_d\, cos(\phi) \tag{7}$$

Equations (6)–(8) define rotor plane normal and torque-producing tangential coefficients. The sectional data [24] instead use chord-normal and chord-tangential directions. For comparison, predictions are projected as CN,ch= Cl cos α + Cd sin α and Ct,ch = Cl sin α − Cd cos α. With θ = twist + pitch, these equal CN,rot cos θ + Ct,rot sin θ and Ct,rot cos θ − CN,rot sin θ. The rotor plane coefficients remain in torque and thrust integration. The coefficient reference in BEM is q = ρW^2/2; the experiment uses corrected stagnation normalization [18]. Without the corresponding QNORM records, their pointwise equivalence cannot be confirmed.

The corresponding sectional loads are

$$p_n = \frac{1}{2}\rho\, W^2\, c\, C_N,\ p_t = \frac{1}{2}\rho\, W^2\, c\, C_t \tag{8}$$

After convergence, integrated thrust (T), torque (Q), and aerodynamic power (P) are obtained from

$$T = B\int_{r_0}^{R} p_n\, dr\ ,\ Q = B\int_{r_0}^{R} p_t r\, dr,\ P = \Omega\, Q \tag{9}$$

Here r_0 = 1.2575 m is the lower aerodynamic integration limit; the hub radius Rh = 0.5083 m enters the hub loss model. Per-blade loads pn and pt have units N m^{-1}. Thus Q = B∫r pt dr has units N m. Blade count and moment arm are included in the numerical integration. Uniform annulus-center evaluation uses midpoint sums Q ≈ BΣr_i pt,i Δr_i and T ≈ BΣp_n,i Δr_i, rather than trapezoidal quadrature. Contributions below r_0 are omitted.

The nondimensional rotor coefficients are

$$C_P = \frac{P}{\frac{1}{2}\rho\, A\, U_\infty^3},\ C_T = \frac{T}{\frac{1}{2}\rho\, A\, U_\infty^2} \tag{10}$$

The swept area is A = πR^2. C_P is the power coefficient, and C_T is the rotor thrust coefficient; both are dimensionless. C_T must not be confused with the sectional tangential coefficient C_t or the chordwise NREL channel CT.

3.1. Prandtl Tip and Hub Loss Correction

The finite number of blades produces a reduction in circulation near the blade tip and hub. This effect is introduced through the combined Prandtl factor $F = F_{tip} \times F_{hub}$, with

$$F_{tip} = \left(\frac{2}{\pi}\right) cos^{-1}\left\{ exp\left[-\frac{B(R-r)}{2\,r\,|sin\,\phi|}\right]\right\} \tag{11}$$

$$F_{hub} = \left(\frac{2}{\pi}\right) cos^{-1}\left\{ exp\left[-\frac{B(r-R_h)}{2\,R_h|sin\,\phi|}\right]\right\} \tag{12}$$

The implementation bounds F = min [1, max(10^{-4}, Ftip Fhub)] and uses max(|sin ϕ|, 10^{-5}) in the Prandtl exponents. Annulus centers avoid endpoint singularities. Floors of 10^{-5}, 10^{-4} and 10^{-3} do not alter the 90-annulus results because the floor is inactive at the sampled centers; this sensitivity does not remove discretization error near the blade ends.

3.2. Induction Update and Buhl High-Induction Correction

For the low-induction branch, the induction factors are updated from the local blade-element coefficients as

$$a = 1/\left[4\,F\frac{sin^2(\phi)}{\sigma\,C_N} + 1\right] \tag{13}$$

$$a' = 1/\left[4\,F\frac{sin(\phi)cos(\phi)}{\sigma\,C_t} - 1\right] \tag{14}$$

When the local thrust loading enters the turbulent windmill state, the classical relation between thrust and axial induction becomes unreliable. The loss-consistent Buhl correction is introduced through the local thrust coefficient as follows:

$$C_{T,loc} = \sigma\,C_N\,(1-a)^2\,/\,sin^2(\phi) \tag{15}$$

For $C_{T,loc} < 0.96\,F$, the classical branch is retained; otherwise, the empirical Buhl branch is used:

$$a = \frac{1}{2}\left[1 - \sqrt{\left(1 - \frac{C_{T,loc}}{F}\right)}\right],\ C_{T,loc} < 0.96F \tag{16}$$

$$a = \frac{18F - 20 - 3\sqrt{C_{T,loc}(50-36F) + 12F(3F-4)}}{36F-50},\ C_{T,loc} \geq 0.96F \tag{17}$$

The branch in Equation (17) inverts $C_{T,loc} = 8/9 + (4F - 40/9)a + (50/9 - 4F)a^2$ [10]. At $C_{T,loc} = 0.96F$, it gives a = 0.4 and joins the classical relation. The implementation uses the algebraically equivalent k = σC_N/(4F sin^2ϕ) branch, with high induction activated at k > 2/3. This treatment applies to the stated turbine branch, rather than general reverse flow.

Both induction factors use constant under-relaxation ω = 0.35, starting from a = 0.3 and a′ = 0. Bounds are −0.5 ≤ a ≤ 0.95 and −0.95 ≤ a′ ≤ 0.95. The numerical solution requires max(|Δa|,|Δa′|) < 10^{-8} and a separately evaluated fixed-point residual < 10^{-8}, with at most 1000 iterations per annulus. All 42 refined model/speed calculations converge; the largest iteration count is 406. A sensitivity study with 90 annuli, 250 iterations, and an update tolerance of 10^{-6} is included in the Supplementary Material. On that grid, tightening the tolerance and using relaxation 0.15, 0.35, or 0.60 changes torque by at most 0.016 N m.

3.3. Rotational Augmentation Models

Rotating blades can retain lift beyond the stall angle of the corresponding stationary airfoil section because centrifugal and Coriolis effects modify the separated boundary layer. The present solver evaluates two empirical rotational augmentation models. In both cases, the corrected lift coefficient is expressed as

$$C_{l,3D} = C_{l,2D} + f_{rot}(r,c,\theta)\,[C_{l,pot} - C_{l,2D}] \tag{18}$$

The implemented potential-lift reference is $C_{l,pot} = \text{clip}\,[2\pi(\alpha - \alpha_0), -2.5, 2.5]$, with angles in radians and $\alpha_0 = -0.38°$. Final coefficients are bounded to $-3 \le C_l \le 3$ and $0.001 \le C_d \le 3$. The model coefficients below describe the engineering implementation used here, including clipping, rather than every variant of the published corrections.

$$f_{rot,Snel} = min[1, 3(c/r)^2] \tag{19}$$

The CH-type expression includes twist attenuation,

$$f_{rot,CH} = clip[2.2\ (c/r)^{1.3}\ cos^4\theta, 0, 1] \tag{20}$$

Snel uses $f = \min\,[1, 3(c/r)^2]$ and modifies lift only, retaining the input drag. CH uses $f = \text{clip}\,[2.2(c/r)1.3\cos^4\theta, 0, 1]$, where θ includes twist and the 3° pitch. In addition to Equation (18), CH modifies drag as $C_{d,3D} = C_{d,2D} + f(C_{d,2D} - 0.0116)$. Both lift and drag therefore contribute to the CH response. No separate radial or angle-of-attack activation gate is used: augmentation follows polar lookup across the modeled span and angle range. The potential-lift and final-coefficient bounds limit, but do not validate, large-angle extrapolation. A lift-only CH sensitivity raises torque RMSE from 204.2 to 547.5 N m, demonstrating that the drag term materially affects the reported ranking.

3.4. Viterna Polar Extrapolation

The solver reads a pre-extended polar rather than regenerating Viterna coefficients during iteration. Equations (21)–(25) describe the standard positive-angle matching construction underlying this input; the complete archived table, including its asymmetric negative-angle and reverse-flow entries, is supplied for exact reproduction. The positive matching boundary is 20.1°, with $C_{l,s} = 0.660$ and $C_{d,s} = 0.3186$; the negative boundary is −20.1°, with $C_{l,s} = -0.560$ and $C_{d,s} = 0.3027$. The archived header lists a nominal stall angle of 15.3°, which is distinct from the central-table endpoint.

$$C_D = B_1 sin^2(\alpha) + B_2\ cos(\alpha) \tag{21}$$

$$C_L = A_1\ sin(2\alpha) + A_2\ cos^2(\alpha)/sin(\alpha) \tag{22}$$

with constants determined from the stall-limit coefficients:

$$A_1 = C_{D,max}/2,\ B_1 = C_{D,max} \tag{23}$$

$$A_2 = \frac{[C_{L,s} - C_{D,max}\ sin(\alpha_s)cos(\alpha_s)]sin(\alpha_s)}{cos^2(\alpha_s)} \tag{24}$$

$$B_2 = [C_{D,s} - C_{D,max}\ sin^2(\alpha_s)]/cos(\alpha_s) \tag{25}$$

For the clamped comparison, $\alpha_c = \min\,[20.1°, \max(-20.1°, \alpha)]$ and both C_l and C_d are evaluated by PCHIP at α_c. The full-angle case queries the archived table over −180° to 180°, with angle bounds enforced by lookup. Snel or CH augmentation is applied after either lookup, using the actual α in the potential-lift reference. The clamping test therefore changes the underlying polar treatment while retaining induction, geometry, grid, and augmentation settings.

The archived aspect ratio is AR = 11, giving $C_{D,max} = 1.11 + 0.018\ AR = 1.308$. At ±90°, the table has $C_l = 0$ and $C_d = 1.308$; at ±180°, $C_l = 0$ and $C_d = 0.1748$. All intervals, including negative angles and ±90° to ±180°, are represented explicitly in the 58-row file and interpolated by PCHIP; no additional negative-angle symmetry is imposed. These endpoint properties apply to the underlying table. Subsequent rotational augmentation can change them, so the framework is not validated for reverse-flow or arbitrary full-angle operation.

3.5. Validation Metrics

The model hierarchy is ranked using root mean square error, mean absolute error, mean bias, and coefficient of determination:

$$RMSE = \sqrt{\left[(1/N) \, \Sigma_{i=1}{}^{N} \left(y_{pred,i} - y_{exp,i} \right)^2 \right]} \tag{26}$$

$$MAE = (1/N) \, \Sigma_{i=1}{}^{N} \, |y_{pred,i} - y_{exp,i}| \tag{27}$$

$$Bias = (1/N) \, \Sigma_{i=1}{}^{N} \, (y_{pred,i} - y_{exp,i}) \tag{28}$$

$$R^2 = 1 - \frac{\Sigma_{i=1}{}^{N} \left(y_{pred,i} - y_{exp,i} \right)^2}{\Sigma_{i=1}{}^{N} \left(y_{exp,i} - \overline{y}_{exp} \right)^2} \tag{29}$$

Here $\bar{y}_{exp} = (1/N)\Sigma_i \, y_{exp,i}$. Subscripts Q, P, C_N, and C_t identify the target variable, not a model identifier or exponent. Positive bias means overprediction. N = 7 for rotor scale metrics and N = 35 for the reported pooled sectional metrics. R^2 is the standard prediction score, not the squared Pearson correlation. It is undefined when experimental variance is zero and negative when squared prediction error exceeds that of the constant experimental mean. With small but nonzero variance, modest absolute errors can produce strongly negative values; sensitivity does not invalidate their interpretation.

Relative error reduction with respect to the 2D baseline is evaluated as

$$\eta_{RMSE} = \left[1 - \frac{RMSE_{model}}{RMSE_{2D}} \right] \times 100\% \tag{30}$$

4. Numerical Implementation and Correction Hierarchy

The hierarchy comprises six cases: 2D without losses, Prandtl, Prandtl–Buhl, Prandtl–Buhl–Snel, Prandtl–Buhl–CH, and Prandtl–Buhl–CH with clamped polar input. Snel and CH are alternatives, not successive corrections. Each case uses identical geometry, atmospheric properties, operating conditions and numerical controls. The independent switches isolate implementation sensitivity; induction still couples the force and momentum responses. Table 3 summarizes the six correction combinations. Figure 1 presents the computational workflow. Figure 2, Figure 3, and Figure 4 compare rotor torque, aerodynamic power, and power coefficient, respectively. Figure 5 ranks the configurations by power RMSE, and Figure 6 compares their post-stall power predictions.

Table 3. Correction combinations evaluated in the validation study.

Model	Correction Content
2D, no losses	Wake rotation and Viterna polar extrapolation; no finite blade loss correction.
Prandtl only	Tip and hub loss factors with the classical low-induction update.
Prandtl + Buhl	Tip/hub losses plus high-induction switching for heavily loaded annuli.
Prandtl + Buhl + Snel 3D	Momentum corrections plus Snel-type rotational lift augmentation.
Prandtl + Buhl + CH stall	Momentum corrections plus CH lift and drag augmentation
CH stall, clamped polar	Prandtl/Buhl and CH; both input coefficients clamped to ±20.1°

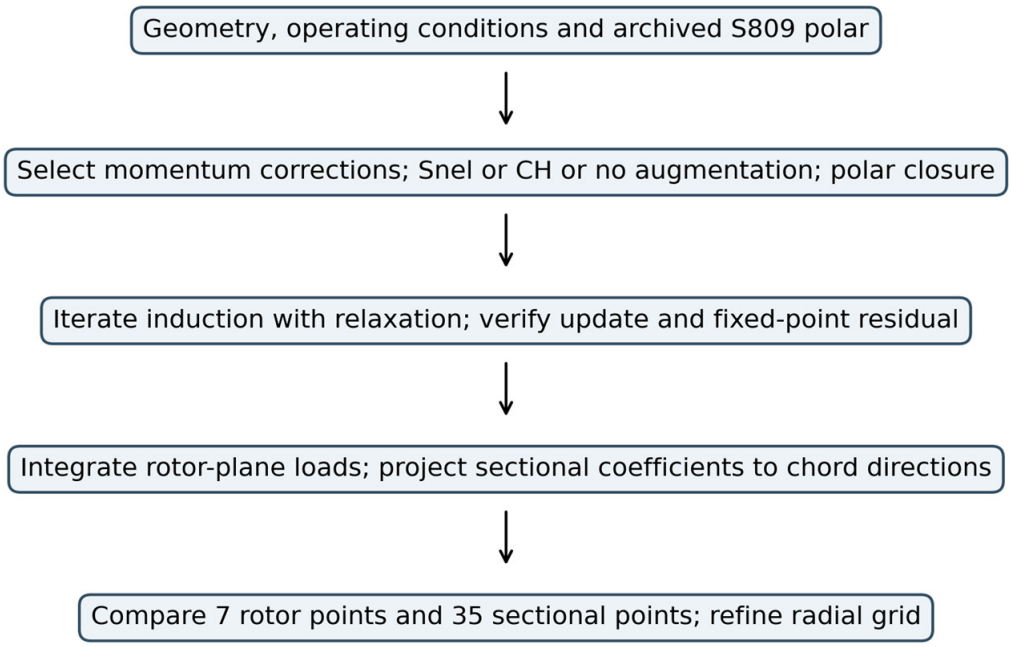


Figure 1. Computational workflow of the modular corrected blade-element momentum (BEM) solver used for the NREL Phase VI validation.

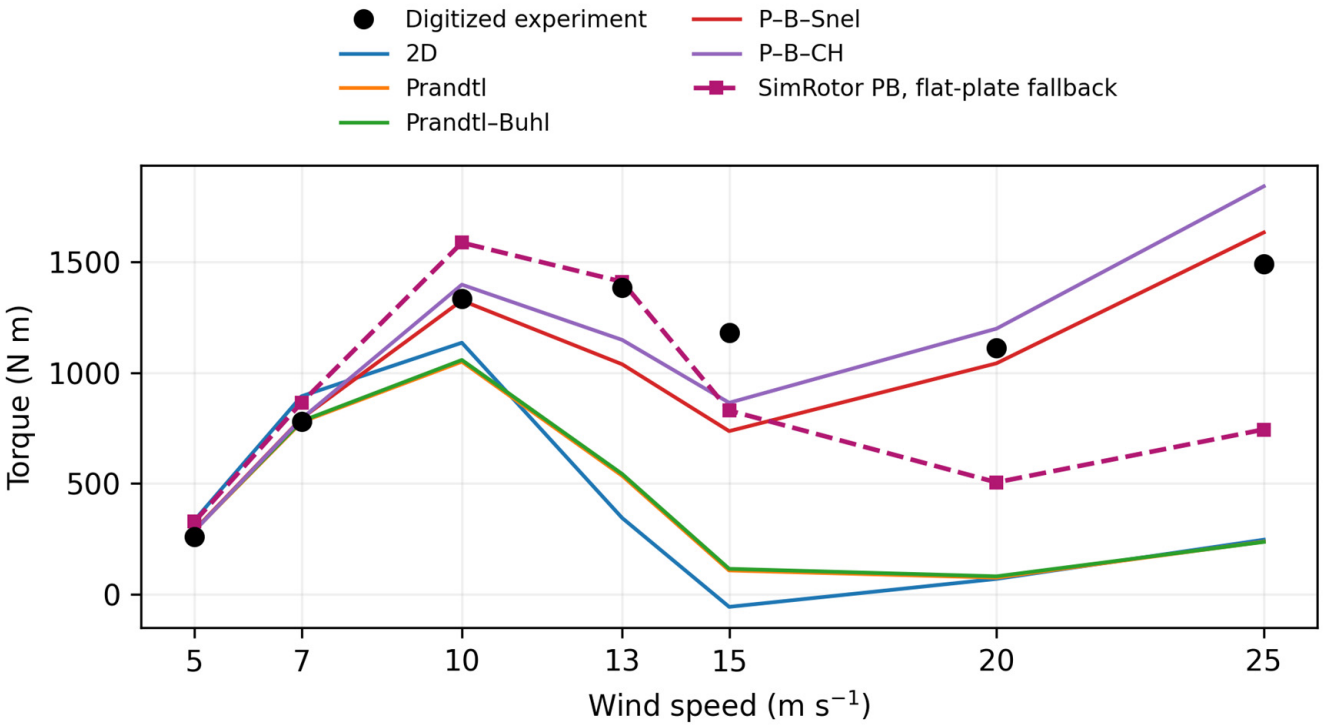


Figure 2. Rotor torque for the correction hierarchy, digitized experimental observations, and external SimRotor study. Dashed magenta curves with square markers denote SimRotor with a bundled XFOIL S809 polar and flat-plate fallback; input differences are described in Section 4.2.

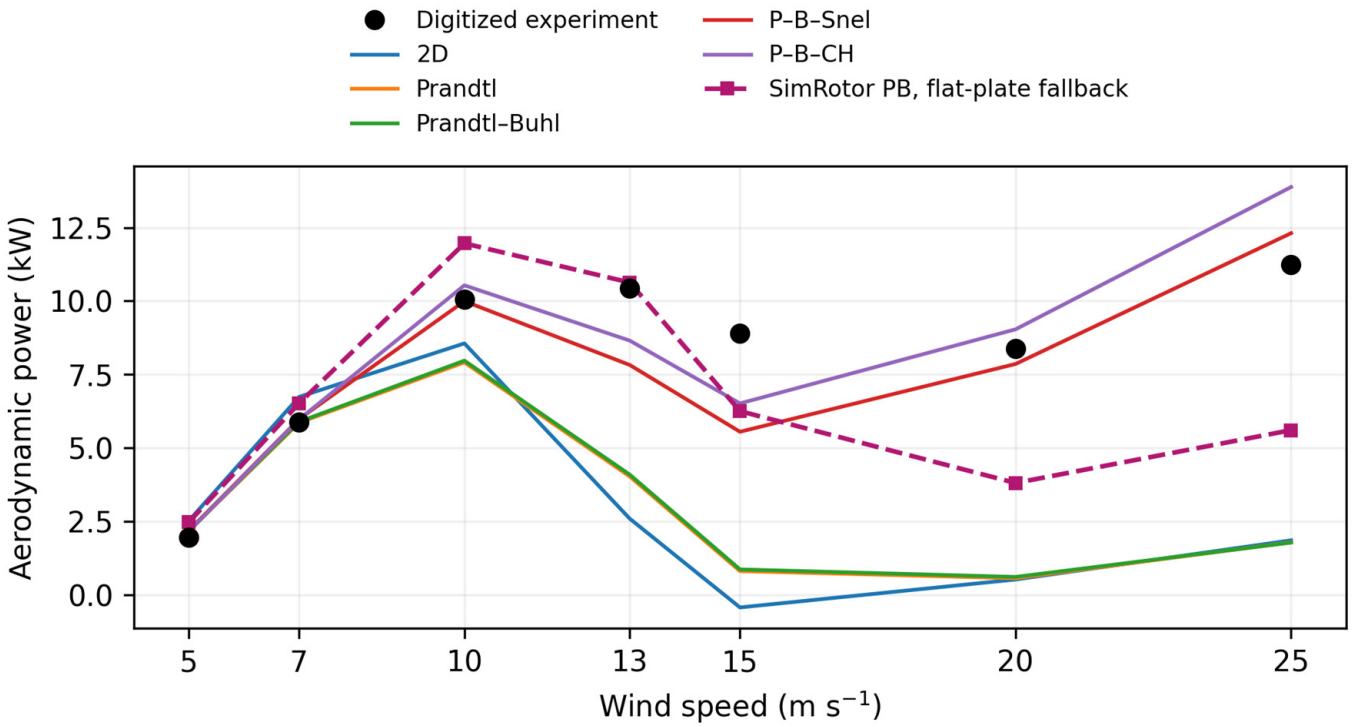


Figure 3. Aerodynamic power derived from torque at 72 rpm for the correction hierarchy, digitized experimental observations, and external SimRotor study. Dashed magenta curves with square markers denote SimRotor with a bundled XFOIL S809 polar and flat-plate fallback; input differences are described in Section 4.2.

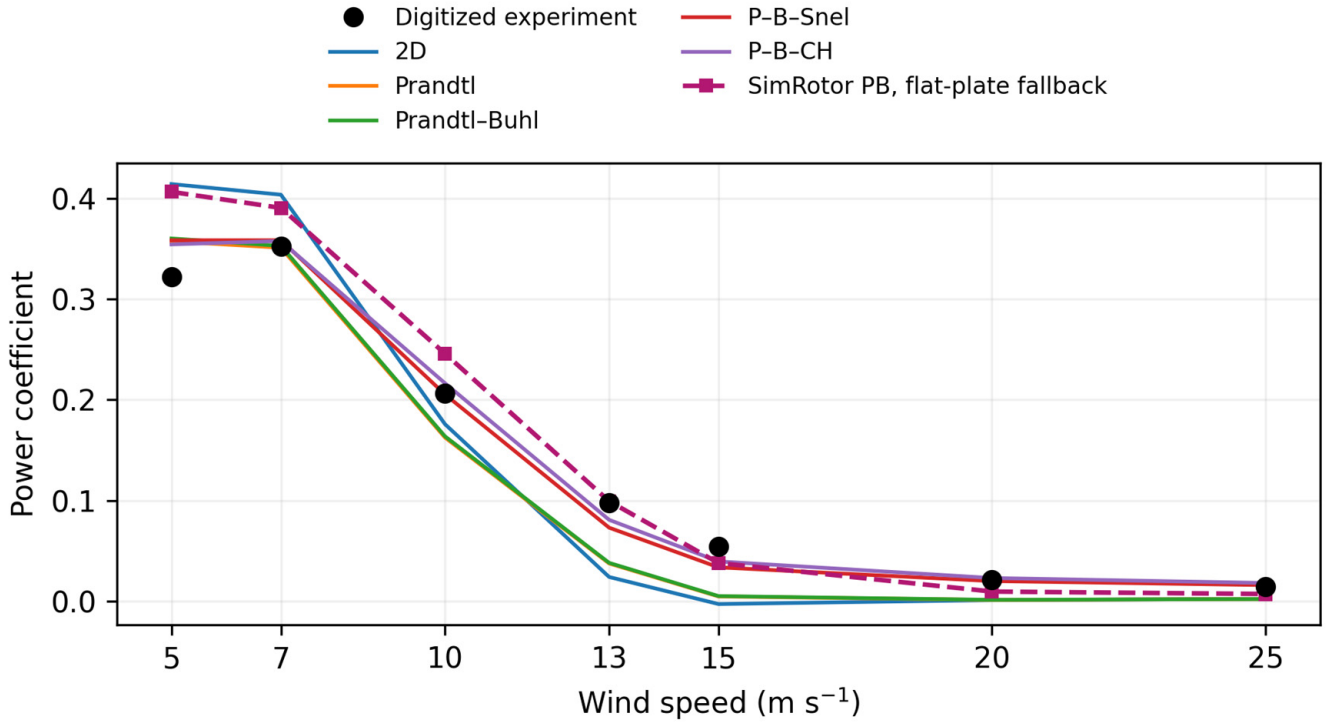


Figure 4. Power coefficient at the seven wind speeds. All values use the same rotor area and freestream reference. Dashed magenta curves with square markers denote SimRotor with a bundled XFOIL S809 polar and flat-plate fallback; input differences are described in Section 4.2.

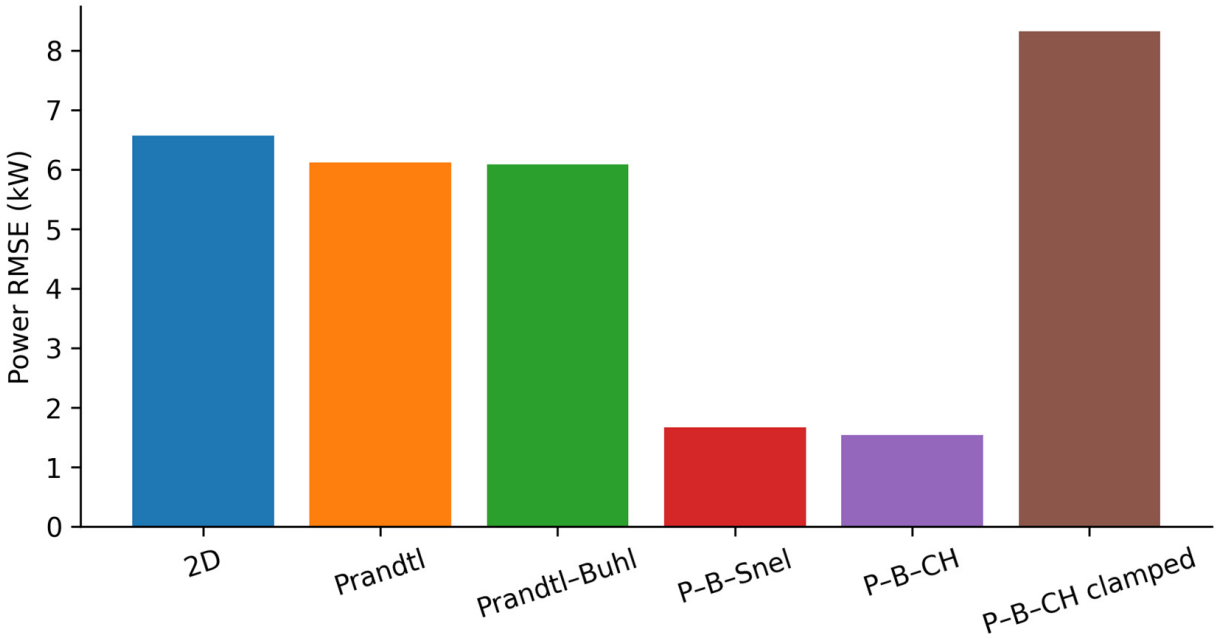


Figure 5. Ranking of correction combinations by power RMSE. The dominant improvement occurs when rotational augmentation is activated.

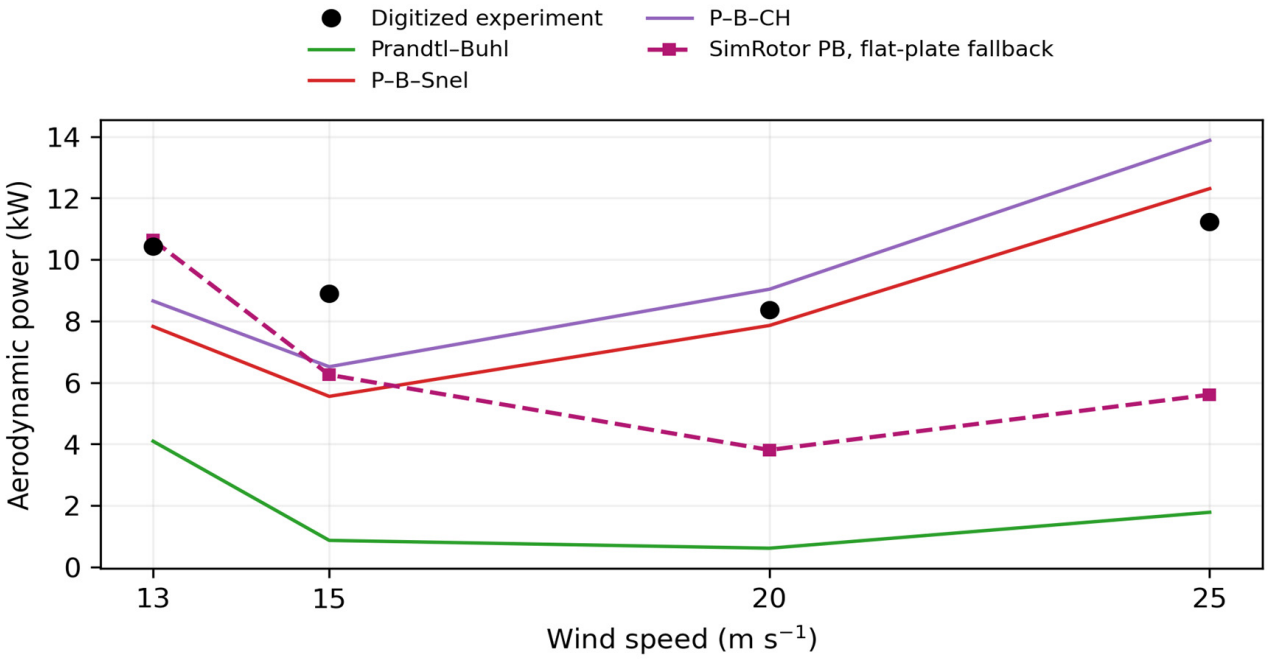


Figure 6. Post-stall aerodynamic power for the Prandtl–Buhl, Snel, and CH configurations, digitized experimental observations, and external SimRotor study. Dashed magenta curves with square markers denote SimRotor with a bundled XFOIL S809 polar and flat-plate fallback; input differences are described in Section 4.2.

Algorithm 1 summarizes the numerical procedure used for each wind speed.

Algorithm 1. Numerical procedure of the modular corrected BEM solver.

1. Read rotor geometry, operating conditions, and airfoil polar data.
2. Interpolate chord and twist to the radial annular grid.
3. Read the archived full-angle polar, or select endpoint clamping for the sensitivity case.
4. For each annulus, initialize a and a'.
5. Compute ϕ, α, W, local solidity, and sectional Reynolds number.
6. Interpolate C_l and C_d and apply the selected rotational augmentation model when activated.
7. Compute C_N, C_t, p_n and p_t.
8. Apply Prandtl loss and update a through the classical or Buhl high-induction branch.
9. Update a′ and a with relaxation; repeat until both update and fixed-point residual criteria pass, or report iteration failure.
10. Integrate sectional loads to obtain T, Q, P, C_T and C_P.
11. Compare rotor predictions with seven torque observations and project sectional coefficients to chord directions for the 35-point comparison.

4.1. Radial Discretization and Numerical Verification

Refinement uses 45, 90, 180, 360, 720, and 1440 annuli, followed by 2880, 5760, and 11,520 annuli. Uniform midpoint integration can show non-monotonic torque changes as local induction branches move relative to annulus centers; iteration convergence alone does not imply radial independence. In particular, 90 annuli do not meet a 1% torque-change criterion in all stalled cases. The main simulations therefore use 2880 annuli. Against 11,520 annuli, the maximum absolute torque difference is 0.640 N m and the maximum relative difference is 0.397%; these maxima occur at different model/speed pairs. Maximum relative thrust difference is 0.009%. Maximum absolute differences at the five comparison stations are 1.02×10^{-7} for chord-normal and 1.26×10^{-7} for chord-tangential coefficients. This satisfies the declared 1% integrated-load and 10^{-5} sectional-coefficient numerical criteria for this dataset; it does not establish model accuracy. Complete pointwise refinement results are provided in the Supplementary Material.

4.2. Reproducibility and External Solver Assessment

The Supplementary Material contains the modular MATLAB (Version 2019b) implementation, rotor geometry, S809 polar, digitized observations, numerical settings and calculation outputs needed to reproduce the correction hierarchy. Source availability is intended to support reproducibility; redistribution and reuse remain subject to the accompanying terms. Computational cost is not quantified because native MATLAB runtime measurements are unavailable. An external BEM study was performed using SimRotor [26] at the same seven wind speeds, 72 rpm, 3° collective pitch, two blades, R = 5.029 m, hub radius 0.5083 m, density 1.225 kg m^{-3}, and dynamic viscosity 1.7894×10^{-5} Pa s. Twenty blade stations spanning 1.2575–5.029 m were imported from the rotor geometry, with tip values evaluated using PCHIP. SimRotor employs a bracketed inflow angle solution with Prandtl tip and hub losses, Buhl high-induction treatment, and drag in both induction equations. Rotational augmentation and yaw skew were disabled. The external calculations used 160 radial elements, a residual tolerance of 10^{-8}, and a maximum of 500 bisection iterations. Native study files and CSV results are supplied with the exported solver identifiers and settings; the platform did not report a software build number.

SimRotor uses its bundled XFOIL S809 polar at Re = 10^6, whereas the present framework uses clean S809 data at Re = 7.5×10^5. The external study also uses the platform's flat-plate fallback outside the polar range, which differs from the archived Viterna-type closure. Figures 2–4 and 6 and Table S1 compare the external predictions with the Prandtl–

Buhl and CH configurations and the digitized experimental observations. SimRotor predicts torques of 327.80, 864.26, 1586.44, 1409.80, 828.99, 504.76, and 743.29 N m at the seven wind speeds, giving torque and aerodynamic power RMSE values of 400.47 N m and 3.019 kW. All 160 elements satisfy the residual tolerance at each speed. Nevertheless, the platform flags the 10–25 m s^{-1} results because they depend on extrapolated coefficients. An 80-element calculation changes torque by up to 4.96% at 20 m s^{-1} (Figure S1), indicating unresolved discretization sensitivity in deep stall. Without the fallback, the highest-speed calculations do not yield admissible converged loads and are excluded from error comparisons. The external study therefore assesses BEM predictions obtained with different aerodynamic inputs; it does not isolate the effect of a single correction or independently verify the CH implementation. Differences in polar source, high-angle treatment, interpolation and solution procedure must be considered when interpreting agreement. Published CFD studies [15,19,20,24,27] provide complementary physical context.

5. Results and Discussion

5.1. Rotor Torque Validation

The uncorrected 2D baseline underpredicts post-stall torque, yielding $RMSE_Q$ = 870.5 N m and mean bias −653.8 N m. Prandtl–Buhl–CH gives the lowest torque RMSE, 204.2 N m, whereas Snel gives 221.7 N m. The 76.5% reduction is a relative error reduction for these seven digitized observations, not a percentage accuracy of the solver.

Prandtl and Prandtl–Buhl reduce torque RMSE to 810.6 and 806.8 N m, respectively, but retain a large post-stall deficit. Momentum corrections alone do not restore sectional loading lost through static-polar stall. Figure 2 and the full operating point CSV show where each configuration improves or deteriorates.

5.2. Aerodynamic Power and Power Coefficient

Power follows torque because $P = \Omega Q$ at the fixed rotational speed $\Omega = 72(2\pi)/60 = 7.5398$ rad s^{-1}. Consequently, $RMSEP = \Omega\, RMSEQ/1000$ and $MAEP = \Omega\, MAEQ/1000$ when power is expressed in kW, while R^2 is unchanged by the positive constant scaling. Torque and power are therefore two presentations of the same rotor scale comparison, not independent confirmations. The recalculated baseline and Prandtl–Buhl power RMSE values are 6.564 and 6.083 kW, respectively.

Table 4 summarizes the rotor-scale error metrics for all six configurations. CH has power RMSE 1.539 kW and bias −0.016 kW; Snel has RMSE 1.671 kW and bias −0.737 kW. CH therefore ranks first by squared error and absolute bias, while Snel has lower MAE (1.135 versus 1.176 kW). The near-zero CH bias reflects cancellation across speeds, rather than uniformly small errors. Geometry-dependent lift retention and drag augmentation plausibly explain the improvement, but this comparison does not independently identify a causal stall-delay mechanism.

Table 4. Rotor scale metrics for all six configurations at 2880 annuli. Torque errors are in N m, power errors in kW; R^2 is dimensionless. Power is derived from torque, so power and torque rankings are identical.

Model	$RMSE_Q$ [N m]	MAE_Q [N m]	$Bias_Q$ [N m]	R^2_Q [−]	$RMSE_P$ [kW]	MAE_P [kW]	$Bias_P$ [kW]	R^2_P [−]
2D	870.5	707.3	−653.8	−3.825	6.564	5.333	−4.929	−3.825
Prandtl	810.6	647.1	−639.0	−3.184	6.112	4.879	−4.818	−3.184
Prandtl–Buhl	806.8	643.0	−634.0	−3.144	6.083	4.848	−4.780	−3.144
P–B–Snel	221.7	150.6	−97.8	0.687	1.671	1.135	−0.737	0.687

Table 4. *Cont.*

Model	$RMSE_Q$ [N m]	MAE_Q [N m]	$Bias_Q$ [N m]	R^2_Q [−]	$RMSE_P$ [kW]	MAE_P [kW]	$Bias_P$ [kW]	R^2_P [−]
P–B–CH	204.2	156.0	−2.1	0.735	1.539	1.176	−0.016	0.735
P–B–CH clamp	1103.5	591.6	553.1	−6.753	8.320	4.460	4.170	−6.753

The power coefficient comparison is also informative. At low wind speeds, the models cluster near the experimental trend because the airfoil operates close to the reliable measured polar range. At higher wind speeds, the power coefficient decreases as stall-dominated operation expands along the blade. Corrected BEM reproduces this decrease while maintaining a more realistic power level than the 2D baseline.

5.3. Post-Stall Power Recovery

The wind speed range from 13 to 25 m s^{-1} is the most discriminating region of the benchmark. In this interval, large parts of the blade operate near or beyond static stall, and the solver becomes highly sensitive to the treatment of sectional lift retention and polar extrapolation. Table 5 isolates this region by comparing predicted post-stall power values for the Prandtl + Buhl model and the two rotational augmentation models.

Table 5. Experimental and predicted aerodynamic power at four post-stall wind speeds. Snel and CH columns include Prandtl and Buhl corrections; all power values are in kW.

U [m s^{-1}]	Experiment [kW]	Prandtl + Buhl [kW]	Prandtl + Buhl + Snel [kW]	Prandtl + Buhl + CH [kW]
13	10.443	4.089	7.822	8.652
15	8.897	0.864	5.549	6.514
20	8.369	0.608	7.856	9.035
25	11.234	1.778	12.309	13.879

The Prandtl–Buhl deficit is particularly large at 15 and 20 m s^{-1}. Both augmentation models restore post-stall power, but CH underprediction at intermediate speeds and overprediction at 25 m s^{-1} partly cancel in its global bias. Table 5 shows four post-stall points, and the supplementary operating point dataset reports all seven speeds for every case. Removing either 13 or 15 m s^{-1} reverses the CH–Snel RMSE ranking; CH remains first in the other five leave-one-speed-out comparisons. Thus, the seven-speed sample supports metric-dependent comparative conclusions, not a statistically universal preference.

5.4. Sectional Normal and Tangential Force Coefficients

The sectional assessment compares five chord-direction coefficients at each of seven speeds. Lift and drag are projected with angle of attack for comparison, while rotor plane projection is used for integration. Table 6 and Figures 7–11 show the comparison in the experimental force directions. This coordinate transformation leaves integrated rotor torque unchanged.

The secondary source identifies coefficients normal and tangential to the chord [24]. Their signs are matched to the reported positive chord-normal and chord-tangential directions. The pressure-derived experimental coefficients and total aerodynamic model coefficients can still differ through skin friction and dynamic pressure normalization. The absence of QNORM records limits the interpretation of this secondary comparison. Consequently, this comparison assesses the digitized coefficients rather than the complete experimental measurement chain.

Table 6. Chord-normal and chord-tangential metrics at 35 sampled points per coefficient. All entries except sample count are dimensionless. Negative R^2 indicates greater squared error than prediction by the experimental mean; small target variance increases its sensitivity.

Model	N	$RMSE_{CN}$	MAE_{CN}	$Bias_{CN}$	$R^2{}_{CN}$	$RMSE_{Ct}$	MAE_{Ct}	$Bias_{Ct}$	$R^2{}_{Ct}$
2D	35	0.543	0.371	−0.269	−0.019	0.085	0.053	−0.031	−0.255
Prandtl	35	0.541	0.361	−0.277	−0.012	0.083	0.050	−0.033	−0.189
Prandtl–Buhl	35	0.541	0.361	−0.277	−0.012	0.083	0.050	−0.033	−0.189
P–B–Snel	35	0.227	0.185	−0.071	0.821	0.217	0.120	0.096	−7.164
P–B–CH	35	0.163	0.126	0.073	0.908	0.134	0.088	0.073	−2.114
P–B–CH clamp	35	0.219	0.165	−0.015	0.835	0.297	0.184	0.170	−14.290

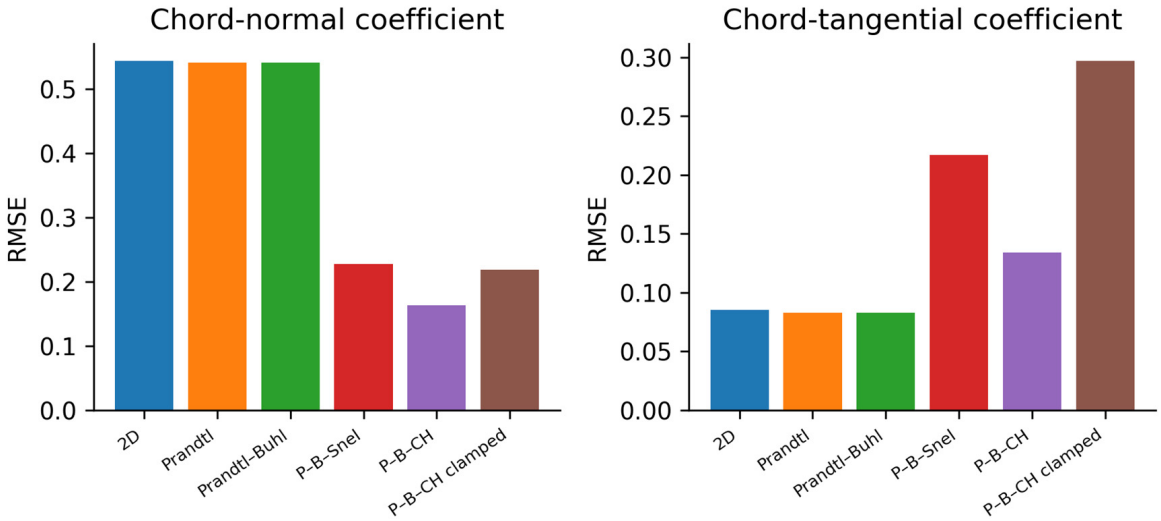


Figure 7. Sectional load RMSE ranking for chord-normal and chord-tangential force coefficients.

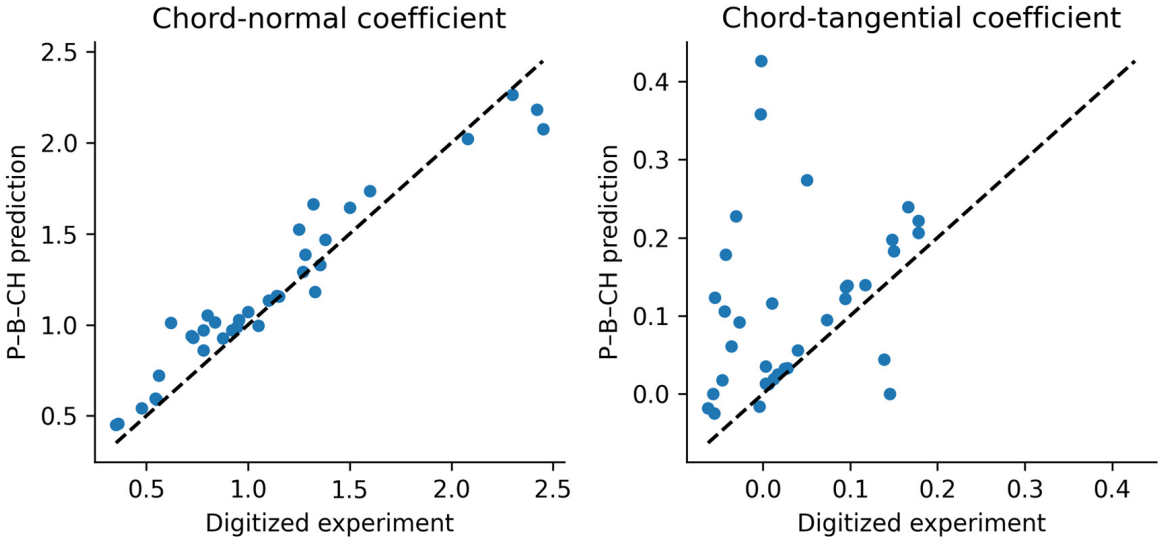


Figure 8. Observed versus predicted chord-normal and chord-tangential coefficients for Prandtl–Buhl–CH at all 35 sampled points. Dashed lines indicate equality; normalization limitations are described in Section 3.

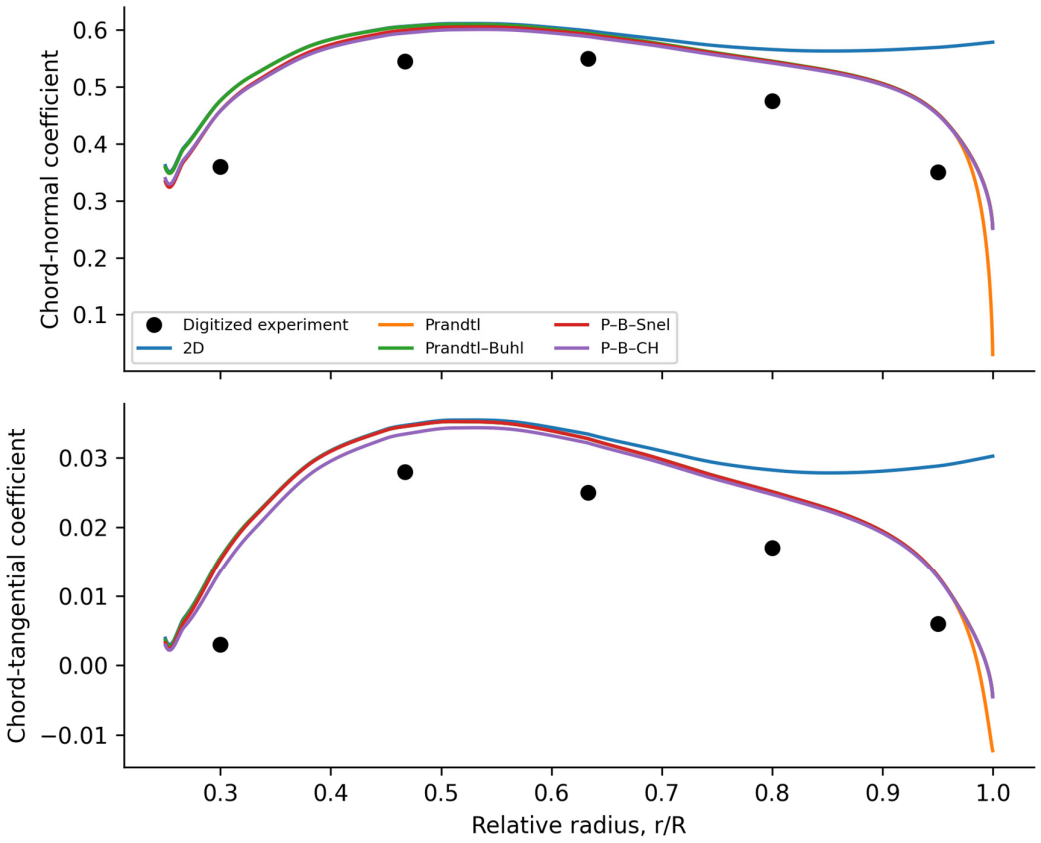


Figure 9. Radial distribution of chord-normal and chord-tangential coefficients at U = 5 m s^{-1}.

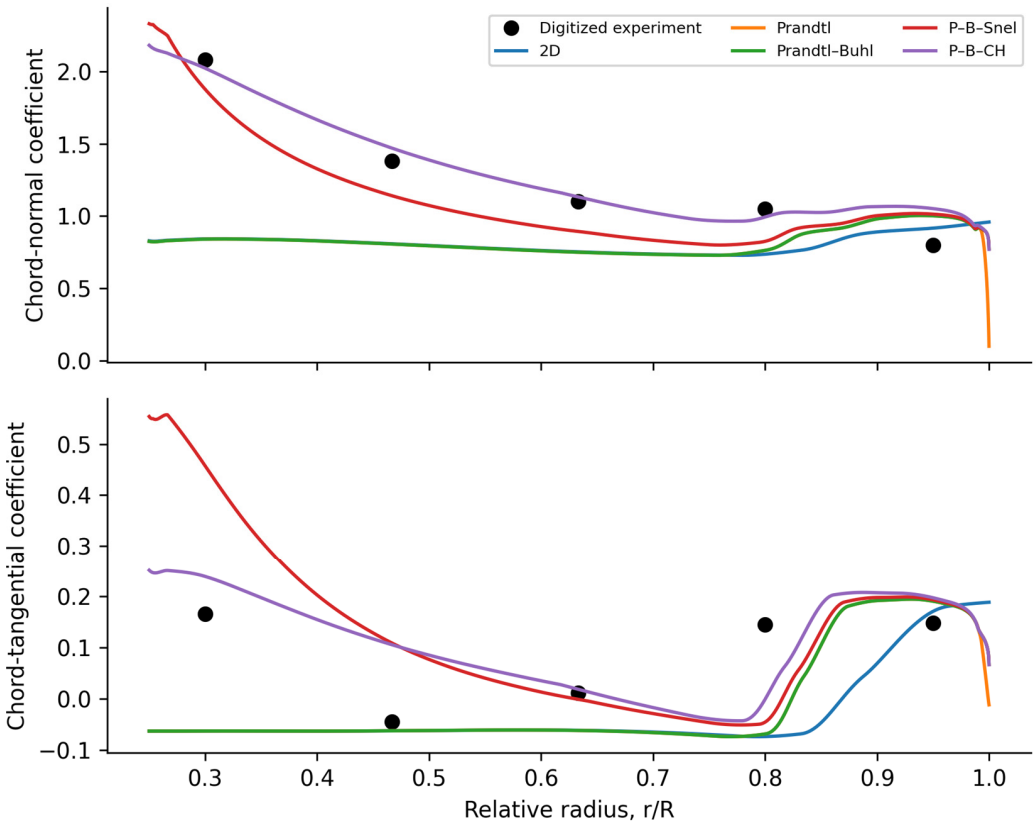


Figure 10. Radial distribution of chord-normal and chord-tangential coefficients at U = 13 m s^{-1}.

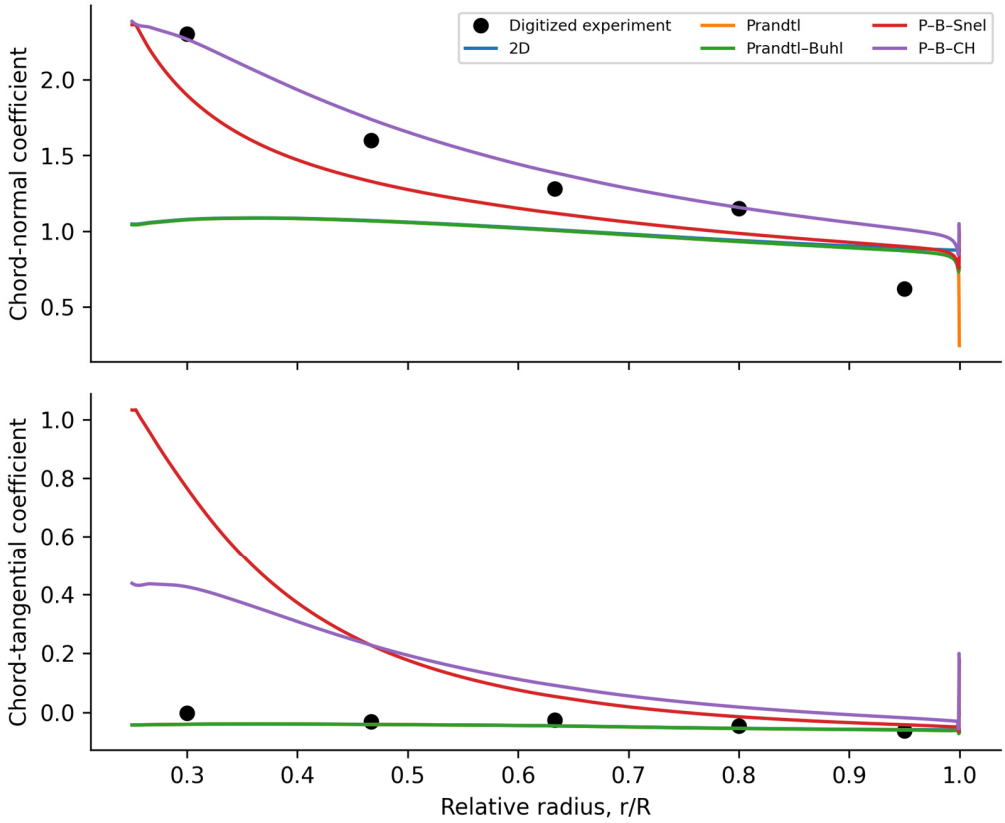


Figure 11. Radial distribution of chord-normal and chord-tangential coefficients at U = 25 m s^{-1}.

CH gives chord-normal RMSE 0.163, MAE 0.126, bias 0.073, and $R^2 = 0.908$. Relative to the 2D baseline RMSE of 0.543, the reduction is approximately 70.0%. Normal loading is improved at sampled stations, although positive bias remains. The five-station dataset cannot resolve all root, tip, or inter-station loading gradients.

Snel gives chord-normal RMSE 0.227 and $R^2 = 0.821$. CH is more accurate by the pooled normal-force metrics, but normal-force performance alone does not determine the torque-producing component or suitability for load prediction.

CH chord-tangential RMSE is 0.134 with $R^2 = -2.114$, compared with 0.083 and −0.189 for Prandtl–Buhl. The negative R^2 indicates that the CH squared error is 3.114 times the squared error of the experimental mean predictor. Low experimental variance makes R^2 sensitive, while the increased RMSE independently confirms poorer tangential agreement. Tangential RMSE is approximately 1.62 times the Prandtl–Buhl value. CH is therefore preferable by global RMSE and normal loading metrics for this dataset, whereas Prandtl–Buhl gives better agreement for the pooled tangential coefficients.

There is no mathematical contradiction between a low pooled chord-tangential coefficient RMSE and poor rotor torque. The pooled metric equally weights 35 sampled coefficient errors, whereas $Q = B\int rqcC_{t,rot}\,dr$ weights continuously distributed rotor plane forces by moment arm, chord and relative dynamic pressure. Chord coefficients also mix normal and tangential rotor components through local twist. Sampling, reference pressure assumptions, and compensating spanwise errors can therefore produce different global and local rankings.

5.5. Radial Load Distributions

The radial distributions provide physical insight into how the correction models modify blade loading. At U = 5 m s^{-1}, the flow is mostly attached, and the correction combinations produce similar radial trends. Differences between models are comparatively small because the airfoil operates near the measured polar range and the induction factors remain moderate.

At U = 13 m s^{-1}, separated flow begins to dominate the inner blade. The 2D and momentum-corrected models lose sectional loading in the inboard and mid-span regions, whereas the rotational augmentation models retain higher C_N and C_t values. This behavior is consistent with delayed stall on rotating blades, where centrifugal pumping and spanwise flow can reduce the severity of separation compared with a stationary 2D section.

At 25 m s^{-1}, CH retains inboard normal loading but overpredicts global torque and power and leaves material chord-tangential error. Steady annular momentum balances and two-dimensional coefficient lookup do not resolve cross-flow boundary-layer pumping, spanwise vortex transport or shedding, and unsteady dynamic stall in deep separation. Weihing et al. [15] examine stalled MEXICO/New MEXICO flow, while Phase VI studies [24,27] provide rotor-specific three-dimensional context. These findings motivate caution rather than a claim that any one omitted mechanism explains the present residual. Dynamic stall states, unsteady inflow/wake treatment, and structural coupling would be needed before extending this solver to aeroelastic loads.

5.6. Effect of Polar Extrapolation

The Viterna/clamped comparison shows sensitivity to high-angle polar handling in the tested solver. Endpoint clamping can prevent a realistic variation of drag and lift beyond the input range, while a full-angle closure supplies explicit high-angle behavior. The comparison remains conditional on identical rotational correction, induction settings and interpolation in the two cases. It does not establish that all other full-angle extrapolation methods would perform worse [14].

Figure 12 compares the archived full-angle S809 lift and drag polars with the endpoint-clamped inputs before rotational augmentation. The clamped CH case gives power RMSE 8.320 kW and torque RMSE 1103.5 N m, compared with 1.539 kW and 204.2 N m for the archived full-angle case. The difference establishes sensitivity to polar closure within this implementation. It neither proves Viterna is the only appropriate closure nor separates extrapolation error from rotational correction behavior at high angles.

The tested hierarchy distinguishes momentum-side corrections, geometry-dependent lift and drag augmentation, and the underlying high-angle table. Because CH modifies drag and is applied after the polar lookup, its behavior cannot be attributed to lift retention alone. High-angle endpoint properties of the archived table do not guarantee the same properties after augmentation.

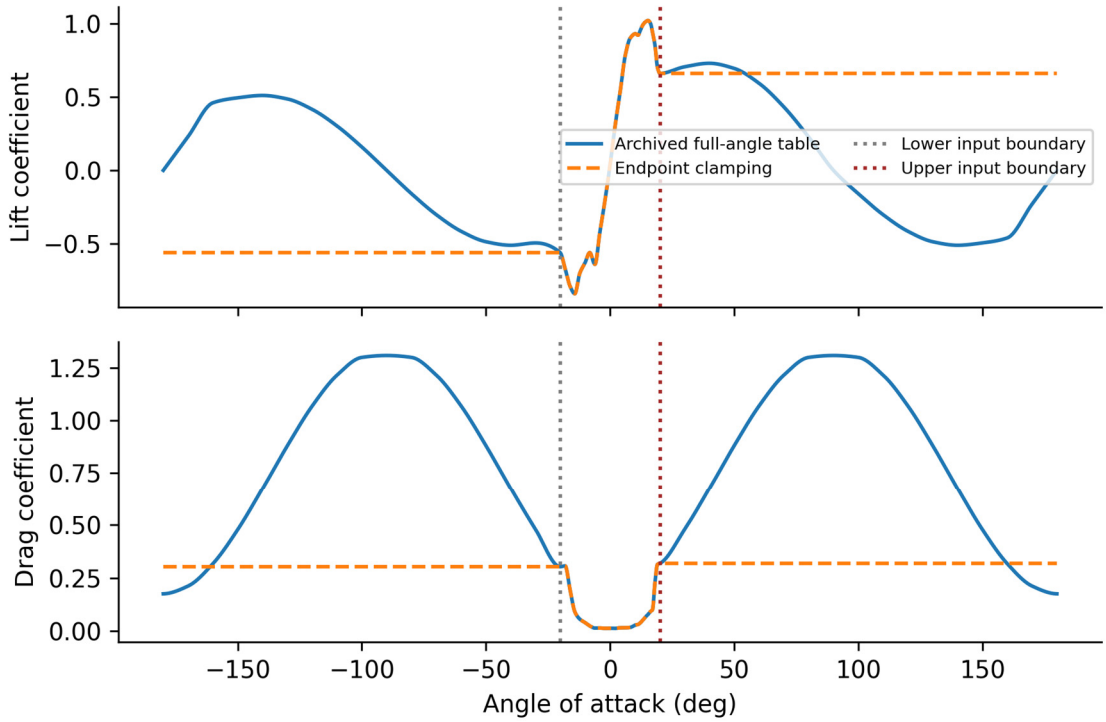


Figure 12. Archived S809 lift and drag coefficients over −180° to 180° (solid curves) and endpoint-clamped coefficients (dashed curves), before rotational augmentation. Vertical dotted lines identify the central input boundaries −20.1° and 20.1°. Both panels share the angle axis.

6. Conclusions

The modular BEM framework quantifies how established momentum corrections, rotational augmentation, and high-angle polar treatment affect NREL Phase VI predictions under steady axial inflow. Combined assessment of integrated performance and sectional loads shows that model preference depends on the target quantity and error metric. The principal findings are as follows:

- The 2D baseline has torque RMSE 870.5 N m and power RMSE 6.564 kW. Prandtl/Buhl improves induction treatment but does not recover post-stall loading without augmentation.
- The 2880-annulus calculation meets the specified numerical criteria against 11,520 annuli: maximum torque and thrust differences are 0.397% and 0.009%, respectively. The 90-annulus calculations do not meet the torque criterion in all stalled cases.
- Prandtl–Buhl–CH has torque RMSE 204.2 N m and power RMSE 1.539 kW, a 76.5% reduction from the baseline. Both the lift and drag augmentation terms contribute to this improvement.
- CH has lower RMSE and absolute bias, while Snel has lower MAE. Removing the 13 or 15 m s^{-1} observation reverses their RMSE ranking, so model preference remains tied to the error metric and tested speeds.
- CH gives chord-normal RMSE 0.163 and $R^2 = 0.908$, but chord-tangential RMSE 0.134 and $R^2 = -2.114$. The negative value indicates worse prediction than the experimental mean and precludes a claim of uniformly reliable sectional loading.
- Sectional predictions are evaluated in the measured chord directions. The fixed-Re polar, unquantified digitization and pressure integration uncertainties, and unavailable raw torque channel and QNORM records limit the strength of experimental validation.
- The archived Viterna-type polar performs better than endpoint clamping for this configuration. Alternative closures and reverse-flow augmentation are not validated by that test.

- The framework supports systematic correction selection for steady rotor-performance assessment. Extension to dynamic stall prediction or aeroelastic loads requires unsteady aerodynamics, wake and inflow modeling, structural coupling, and validation under the relevant operating conditions.

Supplementary Materials: The following supporting information can be downloaded at: https://www.mdpi.com/article/10.3390/pr14213444/s1. The accompanying archive, PhaseVI_Reproducibility_Package.zip, contains the MATLAB source files, exact rotor geometry and S809 polar, digitized experimental observations, operating point errors, convergence and radial refinement studies, and model-ranking sensitivities. Table S1 and the native SimRotor study files document the external 80- and 160-element calculations and their settings. Figure S1 presents the external mesh comparison. Figures 2–4 and 6 are supplied in high-resolution PNG and vector PDF formats, together with MATLAB post-processing instructions. File descriptions, data provenance and reuse terms are provided in the accompanying documentation.

Author Contributions: Conceptualization, M.D.E.B. and T.Z.; Methodology, M.D.E.B.; Software, M.D.E.B.; Validation, M.D.E.B., T.Z., A.B., S.M.A.O., and S.M.R.H.R.; Formal Analysis, M.D.E.B. and T.Z.; Investigation, M.D.E.B., T.Z., A.B., S.M.A.O., and S.M.R.H.R.; Data Curation, M.D.E.B.; Writing—Original Draft Preparation, M.D.E.B.; Writing—Review and Editing, T.Z., A.B., S.M.A.O., and S.M.R.H.R.; Visualization, M.D.E.B.; Supervision, T.Z. All authors have read and agreed to the published version of the manuscript.

Funding: This research received no external funding.

Data Availability Statement: The data presented in this study are available on request from the corresponding author. NREL Phase VI campaign documentation [18], the archived S809 polar [25], and the source figures used for digitization [24] are publicly accessible. The Supplementary Material provides the input data, MATLAB implementation, numerical outputs, and exported external comparison studies.

Acknowledgments: The authors acknowledge the availability of the NREL Phase VI benchmark material and the open literature on BEM correction models, which enable reproducible aerodynamic model validation.

Conflicts of Interest: The authors declare no conflicts of interest.

Nomenclature

Main symbols used in the corrected BEM formulation:

Symbol	Meaning	Symbol	Meaning
a, a'	axial and tangential induction factors	A	rotor swept area [m^2]
B	number of blades	c	local chord [m]
C_l, C_d	lift and drag coefficients	C_N, C_t	normal and tangential sectional force coefficients
C_P, C_T	power and thrust coefficients	F	combined Prandtl tip/hub loss factor
p_n, p_t	normal and tangential sectional loads [N m^{-1}]	P, Q, T	power [W], torque [N m] and thrust [N]
r, R, R_h	local radius, rotor radius and hub radius [m]	U_∞	freestream velocity [m s^{-1}]
W	relative velocity [m s^{-1}]	α	angle of attack [deg or rad]
β	blade pitch angle [deg or rad]	θ	local chord angle: twist + pitch [deg or rad]
ϕ	inflow angle [deg or rad]	ρ	air density [kg m^{-3}]
Ω	rotor angular velocity [rad s^{-1}]	σ	local solidity

References

1. Betz, A. *Wind-Energie und Ihre Ausnutzung Durch Windmuehlen*; Vandenhoeck & Ruprecht: Goettingen, Germany, 1926.
2. Glauert, H. Airplane Propellers. In *Aerodynamic Theory*; Durand, W.F., Ed.; Springer: Berlin/Heidelberg, Germany, 1935; Volume IV, pp. 169–360.
3. Hansen, M.O.L. *Aerodynamics of Wind Turbines*, 3rd ed.; Routledge: London, UK, 2015.

4. Manwell, J.F.; McGowan, J.G.; Rogers, A.L. *Wind Energy Explained: Theory, Design and Application*, 2nd ed.; John Wiley & Sons: Chichester, UK, 2009.
5. Boatto, U.; Bonnet, P.A.; Avallone, F.; Ragni, D. Assessment of Blade Element Momentum Theory-Based Engineering Models for Wind Turbine Rotors Under Uniform Steady Inflow. *Renew. Energy* **2023**, *214*, 307–317. [CrossRef]
6. Zhong, W.; Wang, T.; Shen, W.Z.; Zhu, W.J. A Function Improving Tip Loss Correction of Blade-Element Momentum Theory for Wind Turbines. *Int. J. Sustain. Energy* **2024**, *43*, 2352794. [CrossRef]
7. de Arcos, F.Z.; Wimshurst, A.; Willden, R.H.J.; Pinon, G.; Vogel, C.R. A CFD Study on High-Thrust Corrections for Blade Element Momentum Models. *Wind Energy* **2024**, *27*, 1024–1039. [CrossRef]
8. Selvatici, D.; Stevens, R.J.A.M. Capturing Tip-Corrected Blade Element Momentum Loading with Wind Turbine Models. *Renew. Energy* **2025**, *241*, 122265. [CrossRef]
9. Prandtl, L. *Applications of Modern Hydrodynamics to Aeronautics*; NACA Report 116; NASA: Washington, DC, USA, 1923.
10. Buhl, M.L., Jr. *A New Empirical Relationship Between Thrust Coefficient and Induction Factor for the Turbulent Windmill State*; NREL/TP-500-36834; National Renewable Energy Laboratory: Golden, CO, USA, 2005.
11. Snel, H.; Houwink, R.; Piers, W.J. Sectional prediction of 3D effects for separated flow on rotating blades. In Proceedings of the 18th European Rotorcraft Forum, Avignon, France, 15–18 September 1992.
12. Du, Z.; Selig, M.S. *A 3-D Stall-Delay Model for Horizontal Axis Wind Turbine Performance Prediction*; AIAA Paper 98-0021; American Institute of Aeronautics and Astronautics (AIAA): Reston, VA, USA, 1998.
13. Chaviaropoulos, P.K.; Hansen, M.O.L. Investigating three-dimensional and rotational effects on wind turbine blades by means of a quasi-3D Navier-Stokes solver. *J. Fluids Eng.* **2000**, *122*, 330–336. [CrossRef]
14. Papi, F.; Nocentini, A.; Melani, P.F.; Bianchini, A. Impact of Post-Stall Extrapolation and Rotational-Augmentation Models on the Performance of Stall-Controlled Wind Turbines. In *Proceedings of the ASME Turbo Expo 2022: Turbomachinery Technical Conference and Exposition*; American Society of Mechanical Engineers (ASME): New York, NY, USA, 2022; Volume 11, p. V011T38A014. [CrossRef]
15. Weihing, P.; Cormier, M.; Lutz, T.; Kramer, E. The Near-Wake Development of a Wind Turbine Operating in Stalled Conditions-Part 1: Assessment of Numerical Models. *Wind Energy Sci.* **2024**, *9*, 933–962. [CrossRef]
16. Viterna, L.A.; Corrigan, R.D. Fixed pitch rotor performance of large horizontal axis wind turbines. In *Proceedings of the DOE/NASA Workshop on Large Horizontal Axis Wind Turbines*; NASA Lewis Research Center: Cleveland, OH, USA, 1981.
17. Somers, D.M. *Design and Experimental Results for the S809 Airfoil*; NREL/SR-440-6918; National Renewable Energy Laboratory: Golden, CO, USA, 1997.
18. Hand, M.M.; Simms, D.A.; Fingersh, L.J.; Jager, D.W.; Cotrell, J.R.; Schreck, S.; Larwood, S.M. *Unsteady Aerodynamics Experiment Phase VI: Wind Tunnel Test Configurations and Available Data Campaigns*; NREL/TP-500-29955; National Renewable Energy Laboratory: Golden, CO, USA, 2001.
19. Duque, E.P.N.; Burklund, J.D.; Johnson, W. *Navier-Stokes and Comprehensive Analysis Performance Predictions of the NREL Phase VI Experiment*; AIAA Paper 2003-0355; American Institute of Aeronautics and Astronautics (AIAA): Reston, VA, USA, 2003.
20. Hamlaoui, M.N.; Bouhelal, A.; Smaili, A.; Fellouah, H. An Engineering Approach to Improve Performance Predictions for Wind Turbine Applications: Comparison with Full Navier-Stokes Model and Experimental Measurements. *J. Appl. Fluid Mech.* **2024**, *17*, 1379–1397. [CrossRef]
21. Bouhelal, A.; Ladjal, A.; Smaili, A. Blade Element Momentum Theory Coupled with Machine Learning to Predict Wind Turbine Aerodynamic Performances. In *AIAA SCITECH 2023 Forum*; Paper 2023-1153; American Institute of Aeronautics and Astronautics (AIAA): Reston, VA, USA, 2023. [CrossRef]
22. Cao, G.; Fei, Z.; Vogel, C.R. Uncertainty quantification analysis in the blade element momentum method. *Renew. Energy* **2025**, *250*, 123181. [CrossRef]
23. Kim, H.R.; Printezis, J.A.; Ahrens, J.D.; Seume, J.R.; Wein, L. Characterization of dynamic stall of a wind turbine airfoil with a high Reynolds number. *Wind Energy Sci.* **2025**, *10*, 161–175. [CrossRef]
24. Huque, Z.; Chowdhury, M.S.; Lu, H.; Kommalapati, R.R. Aerodynamic Effect of Winglet on NREL Phase VI Wind Turbine Blade. *Energies* **2024**, *17*, 6480. [CrossRef]
25. National Renewable Energy Laboratory. S809_Cln.dat: Clean OSU S809 Polar at Re = 750000 with Viterna Extension, AR = 11. Archived HARP_Opt WT_Perf/AeroDyn Certification-Test Input. Available online: https://github.com/NatLabRockies/HARP_Opt/blob/master/Source/WT_Perf/v3.05.00a-adp/CertTest/Airfoils/UnsteadyAeroExp/S809_Cln.dat (accessed on 9 October 2026).

26. SimRotor. SimRotor Engineering Platform. Available online: https://simrotor.com/ (accessed on 9 October 2026).
27. Zhu, C.; Qiu, Y.; Feng, Y.; Zhong, W.; Wang, T. Rotational effects on the blade flow of a horizontal axis wind turbine under axial and yawed inflow conditions. *Ocean Eng*. **2023**, *271*, 113764. [CrossRef]

Disclaimer/Publisher's Note: The statements, opinions and data contained in all publications are solely those of the individual author(s) and contributor(s) and not of MDPI and/or the editor(s). MDPI and/or the editor(s) disclaim responsibility for any injury to people or property resulting from any ideas, methods, instructions or products referred to in the content.